Article:

pourkashanian, M., Black, S., Szuhánszki, J. et al. (4 more authors) (2015) LES and RANS of air and oxy-coal combustion in a pilot-scale facility: predictions of radiative heat transfer. Fuel, 151. 146 - 155. ISSN 1873-7153

https://doi.org/10.1016/j.fuel.2015.01.089

LES and RANS of air and oxy-coal combustion in a pilot-scale facility: predictions of radiative heat transfer

Alastair G. Clements[a,*], Sandy Black[a], János Szuhánszki[a], Katarzyna Stęchły[a], Alessandro Pranzitelli[a], William Nimmo[a], Mohamed Pourkashanian[a]

[a]*Energy Technology and Innovation Initiative, University of Leeds, Leeds, LS2 9JT, UK*

Abstract

This study evaluates the use of large eddy simulation (LES) and Reynolds-averaged Navier Stokes (RANS) models for the prediction of turbulent coal combustion under air and oxyfuel environments in a pilot-scale 250 kW_{th} furnace. The furnace is part of the UKCCSRC Pilot-scale Advanced Capture Technology (PACT) facilities and was designed for detailed analysis of the combustion process. The prediction of thermal radiation is validated against experimental measurements under both air- and oxy-firing regimes. Two radiation models were evaluated during the RANS calculations, the widely used weighted sum of grey gases (WSGG) and the full-spectrum correlated k (FSCK) model, while the LES case was calculated using the FSCK radiation model. The results show that the choice in gas radiation model demonstrates only a small change in the temperature and heat flux predictions in the RANS calculations, while the LES solutions are able to achieve better agreement with measured values than the RANS predictions for both air-fired and oxyfuel coal combustion.

Keywords: Large eddy simulation, oxyfuel, computational fluid dynamics, radiation heat transfer

*Corresponding author
Email address: `pmagc@leeds.ac.uk` (Alastair G. Clements)

1. Introduction

The international community is committed to preventing the rise of temperature attributable to anthropogenic climate forcing through the reduction of greenhouse gas (GHG) emissions. Nations have implemented targets to reduce their GHG emissions compared to baseline levels recorded in 1990, with the UK has committing to a 34% reduction in GHG emissions by 2020, which rises to an 80% reduction by 2050. The energy sector will be required to greatly curb its GHG emissions to realise these targets, however with the rising global population, and the industrialisation of developing countries, fossil fuels are still expected to be utilised.

Coal in particular is expected to remain an important global energy resource due to its widespread availability and operating flexibility, however coal-fired combustion is one of the largest global sources of CO_2 emissions [1]. It is necessary to develop carbon capture and storage (CCS) technology so that the benefits of coal-fired energy generation can be realised without violating efforts to reduce CO_2 emissions.

This study focusses on oxyfuel technology for carbon capture. The oxyfuel process for a thermal power station involves firing combustible fuel with a high-purity oxygen stream, which is often diluted with recycled flue gas to control flame temperature and heat transfer. The resulting flue gas from the oxyfuel process contains a high concentration of CO_2 that can be economically purified to a level suitable for transport and storage [2]. Oxyfuel combustion has been demonstrated at small and medium scales [3–5], and is being developed for large scale projects, such as the White Rose CCS[1] and FutureGen 2.0[2] projects.

Oxyfuel technology can be retrofitted to existing combustion facilities, however, with such significant changes to the combustion environment, it is important to develop an understanding of the influence that switching to oxyfuel will have over heat transfer, chemical reactions and flame stability. Furthermore, the

[1] http://www.whiteroseccs.co.uk/

[2] http://futuregenalliance.org/futuregen-2-0-project/

control over the oxygen concentration in the recycled flue gas will provide an additional parameter with regards to combustion efficiency and material corrosion control to optimise against the cost of the oxygen supply, as well as offering further benefits with regards to fuel flexibility [6].

It will be beneficial in the design and optimisation of oxyfuel combustion to be able to predict the influence of operating parameters on the combustion performance. Under oxyfuel, the increase in the concentration of radiatively participating species, namely CO_2 and H_2O, significantly modifies the transfer of thermal radiation [7]. Modelling techniques, such as Computational fluid dynamics (CFD), have been used to predict air-fired combustion facilities, however the novelty of the oxyfuel combustion environment poses challenges to models that are often empirically defined for air-firing. Pilot-scale facilities are important to validate CFD models before they can be applied to larger cases as they provide well controlled environments where detailed experimental measurements can be performed.

This study presents both experimental measurements and numerical solutions for a 250 kW down-fired combustion test facility, which is part of the UK-CCSRC Pilot-scale Advanced Capture Technology (PACT) facilities, operating with both air-fired and oxyfuel coal combustion. The facility was constructed to offer detailed analysis of the combustion process under a range of environments. The measurements of the two combustion modes are used to validate CFD predictions using advanced turbulence and spectral radiation treatment.

2. Combustion test facility

The combustion test facility that is the subject of this study is a vertical down-fired cylindrical furnace, fitted with a scaled 250 kW_{th} burner provided by Doosan Babcock. The burner introduces combustion gases into the furnace through three registers, referred to as the primary, secondary and tertiary, which is illustrated in Figure 2. A central annulus exists for preheating the furnace with a natural gas flame, however this annulus was not used during the measurements.

The coal is transported into the furnace through the primary annulus, with the majority of the combustion oxidant supplied through the secondary and tertiary annuli. The three inlets are swirled with blades fitted into the burner to stabilise the flame and increase the turbulent mixing of the oxidant and fuel.

The cylindrical furnace has an inner diameter of 0.9 m and is 4 m high and is illustrated in Figure 1. The facility is comprised of eight sections that are lined with a 0.1 m thick refractory. The facility was designed to allow for detailed measurements and characterisation of the combustion process under a wide range of operating conditions, and has numerous measurement ports located down the length of the furnace. Each section is 0.5 m high, with the first six sections being water cooled. The top two sections of the furnace contain a number of ports for intrusive and non-intrusive flame measurements. The furnace is maintained at sub-atmospheric pressure by an exhaust fan to ensure safe operation. The same batch of El-Cerrejon coal was fired during the air and oxyfuel combustion measurements in this study. The calorific, proximate and ultimate analyses of the coal are shown in Table 1.

The operating conditions for the air and oxyfuel cases are detailed in Table 2. Both cases were run with the same 200 kW thermal load with the same exit O_2 concentration, measured at 3.3% (dry vol.). The oxyfuel case was fired using an overall 27% (vol.) O_2 concentration, with a balance of CO_2. The O_2 and CO_2 in the oxyfuel case were supplied from liquid storage tanks. The secondary and tertiary gases are preheated using electrical heaters to achieve temperatures that are comparable to values used for utility boilers. The oxygen concentration of the primary gas, which transports the coal, was reduced in the oxyfuel test case to ensure safe operation. The oxygen concentration was enriched in the secondary and tertiary registers to achieve the overall 27% (vol) concentration delivered to the furnace.

Heat transfer to the walls was measured using a Medtherm heat flux transducer. The measurement probe uses a Schmidt-Boelter type sensor with a thermopile fitted at its tip. While exposed to the combustion gases, the device measures the total heat transfer to the wall. The sensor was shielded from convective heat transfer by applying a purge gas of N_2 from the outer circumference of the probe tip at an inward angle to block any combustion gasses from reaching the sensor.

Suction pyrometry was used during the air-fired campaign to measure the in-flame gas temperatures. The suction pyrometer consists of a thermocouple surrounded by a radiation shield. The probe draws the sample gas in at high velocities to intensify the effect of convection and negate the temperature measurement error associated with radiative heat exchange between the thermocouple and its surroundings. Measurements were made across a single radius of the furnace at a time, with the probe being reinserted for different axial locations along the length of the furnace to build up a profile of the gas temperature.

3. Computational modelling

The combustion test facility was modelled using the commercial CFD package ANSYS Fluent version 15. Six cases are considered in total, three for both air and oxyfuel combustion. The three cases consist of two Reynolds-averaged Navier Stokes (RANS) solutions and one large eddy simulation (LES). The RANS solutions are generated using two different models for the radiative properties of the combustion gases; the widely used grey weighted sum of grey gases (WSGG) model, and a more advanced full-spectrum correlated k (FSCK) model, which has been shown to perform well under oxyfuel combustion [8, 9]. The LES for both the air and oxyfuel campaigns are run using the FSCK model.

3.1. Turbulence

RANS models are the most widely employed turbulence treatment due to their relatively low computational cost. Under a steady RANS prediction, transport equations are solved for time-averaged values to calculate the steady-state condition of a system. While extremely useful in predicting flow phenomena, RANS calculations require models to predict all of the scales of turbulence, which can be dependent on the specific geometry and are therefore not easily specified for generic flow.

In contrast to RANS calculations, LES solves the spatially filtered Navier Stokes equations, and numerically resolves the transient flow for the large scales of turbulence. The small scales of turbulence, which can often be assumed to be uniform and isotropic, are modelled. While LES cases often show accurate results for coal combustion [10–13], and allow for the analysis of transient phenomena [13–15], the vastly increased resources required to resolve the transient flow is often a barrier for its use.

In this study the Launder et al. [16] Reynolds stress model was used for the RANS calculation using the pressure strain term and constants proposed by [17]. Reynolds stress models have often performed well at predicting swirling, confined and reacting turbulent flow, as is present in the current case [18, 19]. The WALE sub-grid turbulence model was used for the LES predictions with a time-step of 2×10^{-4}, using a sub-grid turbulent Schmidt number of 0.4, as has been used in other studies [20–22].

All of the cases in this study were run on a hexahedral structured mesh with around three million cells. The dependency of the RANS solutions on the grid size was checked using periodic meshes, with the mesh that had the lowest number of cells, while still producing grid-independent solutions, was used to construct the full 3D grid used in this study. The LES in this study uses an implicit filter width, which is determined by the mesh cell size, and is therefore sensitive to the resolution of the grid. Assuming that at least 80% of the turbulent kinetic energy should be resolved to obtain an accurate LES, a filter width of one twelfth of the characteristic length scale of the energy containing eddies, $\mathcal{L}$, is required [23]. This length scale was estimated from the RANS solutions, using $\mathcal{L} = k^{1.5}/\epsilon$, where k and ϵ are the turbulent kinetic energy and dissipation rate respectively, and the filter width was calculated as $\Delta_w = \sqrt[3]{v_{cell}}$, where v_{cell} is the cell volume. The quality of the grid for LES was evaluated by analysing $\Delta_w/(\mathcal{L}/12)$, and highlighting regions where this value exceeded a ratio of one. This criterion can be too relaxed, and it is often possible to achieve more accurate simulations with further refinements in the grid and filter width. This criterion was satisfied in the majority of the domain, however the grid was not sufficiently resolved in the near burner or the near wall regions, as can be shown in Figure 3. The grid was used despite this deficiency due to the limitations of resources. Wengle and Werner [24] wall functions were also used for the LES case and enhanced wall treatment was used for the RANS calculations so that the mesh did not have to be resolved through the boundary layer. Second order upwind schemes were used for the discretisation of the convective terms in the RANS solutions, while a bounded central differencing scheme was used for the LES, and the solution was advanced in time by the use of an implicit second order scheme. Transient effects at the inlets were neglected in the LES.

3.2. Radiation heat transfer

Calculating radiative heat transfer is challenging due to the spatial, angular and spectral variation in the radiative intensity field. Due to the dominance of thermal radiation at combustion temperatures, separate models that account for the spectral variation in radiative transfer are compared in this study; the grey WSGG method, which is provided by default in Fluent, and the FSCK model, which has been implemented with user-defined functions. This study uses the finite volume method implemented in Fluent (discrete ordinates) to solve radiative transfer in spatial and angular dimensions, due to its superiority in calculating incident radiation at the boundary of the domain [25]. The model is used with a 3×3 angular discretisation for each octant of the solid angle, resulting in 72 ordinates for each control volume. A 4×4 discretisation was tested for the RANS calculation with the grey WSGG model, and the maximum variations in the temperature and incident radiation predictions were less than 2.5% across both the air-fired and oxyfuel cases. The internal emissivity of the refractory-lined walls were assumed to be grey, as mandated by the use of the global models, and were set to a constant value of 0.8.

The grey WSGG method calculates an effective gas absorption coefficient based on the weighted sum of emissivity from fictitious grey gases. The absorption coefficients and the weights of the grey gases are fitted to values of emissivity, which are often calculated from band models or high-resolution spectral databases. The values that are built into Fluent are based on the calculations by Smith et al. [26], which were generated for air-fired combustion, and therefore should not be applied to oxyfuel combustion.

Unlike the grey WSGG method, the FSCK method is not restricted to any specific environment. The FSCK method calculates radiative intensity based on a reordered absorption coefficient against a normalised spectral dimension [27]. Through this manipulation of the radiation transfer equation (RTE), it is possible to accurately calculate radiative transfer with a small number of discretisations in the spectral dimension. In this study a five-point Gauss quadrature was used to calculate radiative heat transfer for the FSCK model, as it has been shown to perform well for oxyfuel conditions [9]. While a five-band quadrature is small compared to line-by-line and band models, it still requires a significant increase in the memory and CPU-time requirements of the calculation over the more widely-used grey WSGG method. The FSCK implementation considered gas absorption and emission from CO_2, H_2O and CO, with the k-distributions themselves being calculated from the narrow-band k-distributions from Cai and Modest [28], using the mixing scheme by Modest and Riazzi [29]. Further details of the FSCK implementation and validation can be found in Clements et al. [9].

Turbulent fluctuations in temperature and gas concentrations can differ significantly from statistically averaged or spatially filtered values. Due to the fourth power relationship between temperature and radiative emission, these turbulent structures significantly increases the amount of radiation emitted from participating gases, as well as also increasing the gas absorptivity through the absorption coefficient's dependence on local thermodynamic properties [30]. The accuracy of the turbulence prediction can significantly influence the calculation of radiative intensity that, through the energy equation, will also modify the fluid dynamics, which is known as turbulence-radiation interaction (TRI). While LES resolves some of the TRI, it is unclear whether it is necessary to further resolve TRI at sub-grid scales [31, 32]. This study did not utilise a sub-grid model for radiation.

In addition to the gas participation, fuel, char, soot and ash particles all contribute to radiative transfer. Due to exothermic reactions on the particle surface, char particles are often over 200 K hotter than the surrounding gas [33], and therefore contribute significantly to the emission of radiation. Fly ash can also have a significant effect on radiation emission and scattering [34]. While the sensitivity of the results to the particle radiation properties is acknowledged, this study only used typical spectrally constant values for the particle absorption efficiency of 0.9, and a low particle scattering efficiency of 0.01 to compensate for the use of an isotropic scattering phase function. Grey particle emission in the FSCK model was included for each band by scaling the radiative source by the emissivity weight function evaluated at the particle temperature, while grey particle absorption was added to the local k-distribution values. Due to their high emissivity, coal-derived soot particles were also accounted for using the model by Brown and Fletcher [35]. Soot radiative properties were treated with the default treatment for the WSGG model in Fluent, but non-grey soot participation was included in the FSCK model using the correlations by Chang and Charalampopoulos [36] to calculate the soot absorption coefficient at the narrow-band centres when constructing the full-spectrum k-distributions.

3.3. Particle combustion

Coal particles are tracked within a Lagrangian frame, and are coupled to the Eulerian fluid phase through appropriate source terms. Turbulent dispersion of the particles in the RANS cases were modelled using the discrete random walk model that is available in Fluent, which tracks the same physical particle numerous times while stochastically perturbing the particle's velocity based on the local turbulent kinetic energy of the fluid domain. Unsteady particles were tracked with the fluid in the LES without any stochastic variations, with the assumption that the sub-grid scales did not influence the particle motion. Unlike in the fluid phase, particle temperatures are not averaged during the tracking, and peaks in temperatures will be correctly accounted for in the particle emission terms for both the RANS and LES cases.

The combustion of a coal particle is modelled as a series of contiguous steps; inert heating, drying, devolatilisation, heterogeneous char combustion and inert heating/cooling of resultant ash particles. The process of devolatilisation and char combustion is expected to differ between air and oxyfuel combustion [37], however, in the absence of any empirically derived rates for the precise combustion conditions being modelled in this study, the same combustion model parameters were used for both the air and oxyfuel cases.

Coal volatiles are modelled as an empirically defined species, derived from the proximate and ultimate analysis of the coal, assuming that the volatile yield at high temperatures is 1.57 times greater than the value measured in the proximate analysis. The volatile evolution from the coal is modelled using a single Arrhenius rate. Char combustion is modelled using the intrinsic model [38], with the char combustion products being treated as CO. The parameters for the devolatilisation and char combustion models were obtained from Pranzitelli et al. [39].

3.4. Homogeneous combustion

The gas-phase combustion of volatile matter and CO released from char combustion was modelled using the eddy-dissipation model [40], which assumes that the rate of combustion is only limited by the turbulent mixing of reactants. The eddy dissipation model calculates the net production rate of a species due to a reaction r as the minimum of the reactant dissipation, $R_{\mathrm{R},r}$, and the dissipation of product species, $R_{\mathrm{P},r}$, which are calculated as

$$R_{\mathrm{R},r} = \nu_{r,i} M_{w,i} A \rho \frac{1}{\tau} \min_{\mathrm{R}} \left(\frac{Y_{\mathrm{R}}}{\nu_{i,\mathrm{R}} M_{w,\mathrm{R}}} \right) \tag{1}$$

$$R_{\mathrm{P},r} = \nu_{r,i} M_{w,i} A B \rho \frac{1}{\tau} \frac{\sum Y_{\mathrm{P}}}{\sum_{j}^{N_r} \nu_{r,j} M_{w,j}} \tag{2}$$

Where R and P denote reactant and product species respectively, $\nu_{r,i}$ is the stoichiometric coefficient of species i in reaction r, $M_{w,i}$ is the molecular weight of species i, ρ is the gas density, τ is the eddy mixing time scale, N_r is the number of reactions, Y denotes mass fraction and A and B are constants. The eddy mixing time scale is taken as k/ϵ in the RANS calculations, and is calculated as the reciprocal of the strain rate for the LES cases. A two-step reaction mechanism was used, where volatile gas species are first oxidised to CO, H_2O, N_2 and SO_2, and the CO is further oxidised to CO_2. The mixing rate parameters for the eddy-dissipation model were taken from values recommended for swirling, confined coal flames [41], using the same values for the RANS and LES cases, where A is set to 0.5 and 0.7 for volatile and CO combustion respectively, and B is set to 0.5.

4. Results and discussion

All of the CFD calculations were run using 64 CPU cores, and took 2 days, 3 days and 30 days to complete for the RANS calculation with the WSGG model, RANS calculation with the FSCK model, and the LES cases respectively. Each LES case was run to compute four seconds of simulation time before statistics were initialised, to account for the residence time of the gas within the measured domain, and were run for a further one second while gathering time-averaged temperature, heat flux and exit gas composition data, until statistical convergence. The LES cases contained roughly eight million particles when the domain was filled.

Figures of the temperature distribution for the RANS cases, as well as instantaneous and time-averaged LES results, can be seen in Figures 4 and 5 for the air and oxyfuel case respectively. The instantaneous temperature distributions reveal the resolution of turbulent structures with regions of higher temperatures compared to the mean flow field. The time-averaged LES results show a much smother temperature distribution than the RANS predictions, with a narrower flame that is rooted inside the quarl.

Figure 6 plots the radial distribution of temperature near to the burner for the air-fired case, comparing the CFD results to suction pyrometry measurements. The plots also compare the predictions against a RANS case without calculating radiative heat transfer, which shows that radiation is responsible for over 400 K difference in the gas temperature, however, as can be seen in the temperature distributions as well (Figures 4 and 5), there is very little difference in the temperature predictions between the two radiation models for the RANS cases. In all three cases, the predicted temperature shows the most deviation from the measured data close to the burner, around 0.15 m from the centre of the furnace. The CFD calculations predict a low rate of mixing between the inlet streams and the combustion gases, resulting in a significant under-prediction of the temperature near the burner. The time-averaged velocity predictions for the air-fired case in the near-burner region, shown in Figure 7, show that the RANS predictions are very similar, however the LES shows greater variation across the radial direction in the external recirculation zone. A similar trend is also visible in the distribution of participating species, Figure 8, where the LES calculation produces much smoother profiles, while the RANS predictions are similar to each other. The LES calculation shows a much smoother variation in the temperature profile, with a higher minimum value, however, there is still a deviation from the experimental data. This near-burner region of the burner has been identified as being likely to be under-resolved, which is caused by the high velocities of the oxidiser streams. It is expected that reducing the cell size in this region, and therefore resolving the smaller length scales of turbulence, will improve the predictions of turbulent mixing, however the RANS simulations, which have been tested for grid dependency, will remain the same. Further downstream of the burner, past 575 mm from the exit of the quarl, the temperature measurements and predictions show a reasonably uniform profile, with the LES and RANS calculations producing similar temperatures.

The temperature profiles for the oxy-27 case, Figure 9, show similar trends to the air-fired case; the RANS predictions are very similar in their temperature distribution, with the LES case predicting a much smoother profile. As with the air-fired results, the RANS calculations without accounting for radiative transfer increases the gas temperature predictions by roughly 400 K, further demonstrating the importance of considering radiation. Additionally, the oxyfuel case also shows similar predictions between the LES and RANS results when the temperature profile becomes more uniform at 575 mm from the quarl exit. The time-averaged predictions of velocity in the oxyfuel case, Figure 10, show similar trends to the air-fired case, however the recirculation in the centre of the furnace is predicted to be stronger in the LES case, which draws in a greater concentration of CO_2 close to the burner, which can be seen in Figure 11.

Comparisons between predicted and measured values of surface incident radiation are shown in Figures 12 and 13 for air and oxy-27 respectively. Under air-fired conditions the two RANS cases over-predict the surface incident radiation, with the FSCK model providing a small improvement over the WSGG predictions. The LES results for surface incident radiation, although showing a similar trend to the RANS predictions, are significantly lower than the RANS results, and are much closer to the experimental measurements. These results agree with other LES and RANS by Edge et al. [14], which showed an over-prediction in surface incident radiation for RANS results, but a very good agreement with LES calculations for a similar Doosan Babcock triple-staged low-NO_x burner. The combination of these findings suggest that the improved treatment of flow turbulence with this burner design provide significantly better predictions with regards to the calculation of surface incident radiation.

The reduced prediction of incident radiation in the LES cases, despite the simulation resolving highly-emitting hot eddies, may be related to the temperature predictions, specifically by analysing the temperature distributions shown in Figures 4 and 5. The figures illustrate that the RANS calculations predict peaks in gas temperature close to the furnace wall, while the LES calculations show higher temperature peaks near the centre of the furnace, which is highlighted by the instantaneous LES results. The location of the peak temperatures in the centre of the domain effectively increases the path-length from the radiation source to the wall significantly, influencing the heat flux at the wall surface. Since the verification of radiative heat transfer prediction is generally measured at the wall, this highlights the importance of predicting the correct flame shape and transient effects of the flame. The sensitivity of the spectral radiation models for the LES calculations should be considered in a further study, to determine whether this increase in radiative path influences the impact over the choice of radiation model.

The LES calculations of air-fired combustion fail to predict the peak in surface incident radiation that was measured in the experiments near 0.7 m from the quarl exit. It is believed that this region, where there is a significant number of combusting char particles, will be sensitive to the correct treatment of particle radiative properties, and this discrepancy could be explained by the simplistic approach used for these values. The measurements of the oxy-27 combustion case do not demonstrate the same peak as the air-fired case, and the LES predictions show a much closer agreement to the measurements. The agreement between the WSGG and the FSCK models in both cases, despite the significant reduction in the temperature prediction from the case when radiation is neglected, suggest that the influence of spectrally constant radiative quantities, such as the particle and refractory wall properties, dominate how radiation is transferred in these cases. In future work it will be important to understand the sensitivity of calculations to more-realistic non-grey radiative properties, and how this influences the predictions from different spectral radiation models.

5. Summary and conclusions

This study compared the influence of a gas radiation model between two RANS cases and a LES case for both air-fired and oxyfuel coal combustion with measurements at a 250 kW pilot-scale facility. The LES results show greater agreement with experimentally measured values than the RANS predictions in the cases studied. The LES predicts greater turbulent mixing of the inlet streams near the burner, which is an important region of practical interest of burner performance with regards to pollutant formation. The RANS calculations using different spectral radiation models demonstrated similar predictions for the two cases that were studied. Further work may investigate the influence of using non-grey radiative properties with a spectral radiation model, such as the FSCK model, over using the more widely adopted grey radiative properties.

The LES results showed greater agreement with experimental measurements for surface incident radiation, predicting lower values than the RANS calculations. While the computational demands for LES are high, roughly ten times that of a RANS on the same computational grid, there is a noticeable increase in the agreement with experimental measurements in the solution, especially in the near burner region, even though the turbulence is under-resolved in this region, and further work should investigate whether an improved resolution will produce greater agreement with measured values. LES predictions are promising, and with further improvement in computational power it will be possible to further resolve the turbulence in similar combustion cases, which should improve the accuracy of predictions, as well as providing other beneficial comparisons with physical phenomena, such as analysis of flame dynamics or statistics on length- and time scales.

Acknowledgements

Financial support by E-ON/OXYCAP-UK project (agreement n. EP/G062153/1) and RCUK-China (agreement n. EP/G063451/1). The authors would also like to thank Prof. Michael Modest for providing the Spectral Radiation Calculation Software (SRCS) that was used to generate the full-spectrum k-distribution parameters for this work.

References

[1] G. Blanco, R. Gerlagh, S. Suh, J. Barrett, H. de Coninck, C. F. D. Morejon, R. Mathur, N. Nakicenovic, A. O. Ahenkorah, J. Pan, H. Pathak, J. Rice, R. Richels, S. J. Smith, D. Stern, F. L. T. P. Zhou, R. Andres, G. Baiocchi, M. Hanemann, M. Jakob, P. Kolp, E. la Rovere, T. Michielsen, K. Nansai, M. Rogner, S. Rose, E. Santalla, T. Wiedmann, T. Wilson, D. Ürge-Vorsatz, M. Gomes, A. Verbruggen, J. Bergesen,

R. Madhusudanan, Drivers, Trends and Mitigation, in: IPCC Fifth Assessment Report, chap. 5, Intergovernmental Panel on Climate Change, 2014.

[2] V. White, L. Torrente-Murciano, D. Sturgeon, D. Chadwick, Purification of oxyfuel-derived CO_2, International Journal of Greenhouse Gas Control 4 (2) (2010) 137 – 142, ISSN 1750-5836, doi: http://dx.doi.org/10.1016/j.ijggc.2009.07.004, the Ninth International Conference on Greenhouse Gas Control Technologies.

[3] N. Aimard, M. Lescanne, G. Mouronval, C. Prèbendè, The CO_2 pilot at Lacq: An integrated oxycombustion CO_2 capture and geological storage project in the South West of France, in: International Petroleum Technology Conference, 2007.

[4] L. Strömberg, G. Lindgren, J. Jacoby, R. Giering, M. Anheden, U. Burchhardt, H. Altmann, F. Kluger, G.-N. Stamatelopoulos, Update on Vattenfall's 30 MWth oxyfuel pilot plant in Schwarze Pumpe, Energy Procedia 1 (1) (2009) 581 – 589, ISSN 1876-6102, doi:10.1016/j.egypro.2009.01.077.

[5] T. Uchida, T. Goto, T. Yamada, T. Kiga, C. Spero, Oxyfuel combustion as CO_2 capture technology advancing for practical use - Callide Oxyfuel Project, Energy Procedia 37 (2013) 1471 – 1479, ISSN 1876-6102, doi: http://dx.doi.org/10.1016/j.egypro.2013.06.022.

[6] J. P. Smart, G. S. Riley, On the effects of firing semi-anthracite and bituminous coal under oxy-fuel firing conditions, Fuel 90 (8) (2011) 2812 – 2816, ISSN 0016-2361, doi:http://dx.doi.org/10.1016/j.fuel.2011.02.032.

[7] T. Wall, Y. Liu, C. Spero, L. Elliott, S. Khare, R. Rathnam, F. Zeenathal, B. Moghtaderi, B. Buhre, C. Sheng, R. Gupta, T. Yamada, K. Makino, J. Yu, An overview on oxyfuel coal combustion – State of the art research and technology development, Chemical Engineering Research and Design 87 (8) (2009) 1003 – 1016, ISSN 0263-8762, doi:10.1016/j.cherd.2009.02.005.

[8] R. Porter, F. Liu, M. Pourkashanian, A. Williams, D. Smith, Evaluation of solution methods for radiative heat transfer in gaseous oxy-fuel combustion environments, Journal of Quantitative Spectroscopy and Radiative Transfer 111 (14) (2010) 2084 – 2094, ISSN 0022-4073, doi: 10.1016/j.jqsrt.2010.04.028.

[9] A. G. Clements, R. Porter, A. Pranzitelli, M. Pourkashanian, Evaluation of FSK models for radiative heat transfer under oxyfuel conditions, Journal of Quantitative Spectroscopy and Radiative Transfer 151 (2015) 67 – 75, ISSN 0022-4073, doi:http://dx.doi.org/10.1016/j.jqsrt.2014.09.019.

[10] M. Gharebaghi, R. Irons, L. Ma, M. Pourkashanian, A. Pranzitelli, Large eddy simulation of oxy-coal combustion in an industrial combustion test facility, International Journal of Greenhouse Gas Control 5, Supplement 1 (2011) S100 – S110, ISSN 1750-5836, doi:10.1016/j.ijggc.2011.05.030.

[11] B. M. Franchetti, F. C. Marincola, S. Navarro-Martinez, A. M. Kempf, Large Eddy simulation of a pulverised coal jet flame, Proceedings of the Combustion Institute 34 (2) (2013) 2419 – 2426, ISSN 1540-7489, doi: http://dx.doi.org/10.1016/j.proci.2012.07.056.

[12] G. Olenik, O. Stein, A. Kronenburg, LES of swirl-stabilised pulverised coal combustion in IFRF furnace No. 1, Proceedings of the Combustion Institute ISSN 1540-7489, doi:http://dx.doi.org/10.1016/j.proci.2014.06.149.

[13] M. Rabaçal, B. M. Franchetti, F. C. Marincola, F. Proch, M. Costa, C. Hasse, A. M. Kempf, Large Eddy Simulation of coal combustion in a large-scale laboratory furnace, Proceedings of the Combustion Institute ISSN 1540-7489, doi:http://dx.doi.org/10.1016/j.proci.2014.06.023.

[14] P. Edge, S. Gubba, L. Ma, R. Porter, M. Pourkashanian, A. Williams, LES modelling of air and oxy-fuel pulverised coal combustion – impact on flame properties, Proceedings of the Combustion Institute 33 (2) (2011) 2709 – 2716, ISSN 1540-7489, doi:10.1016/j.proci.2010.07.063.

[15] S. Black, J. Szuhánszki, L. Ma, D. Ingham, M. Pourkashanian, LES of a 250kW oxy-coal burner: an investigation into flame stability, in: 3rd Oxyfuel Combustion Conference, 2013.

[16] B. E. Launder, G. J. Reece, W. Rodi, Progress in the development of a Reynolds-stress turbulence closure, Journal of fluid mechanics 68 (3) (1975) 537–566.

[17] M. M. Gibson, B. E. Launder, Ground effects on pressure fluctuations in the atmospheric boundary layer, Journal of Fluid Mechanics 86 (3) (1978) 491–511, doi:http://dx.doi.org/10.1017/S0022112078001251.

[18] R. Weber, B. M. Visser, F. Boysan, Assessment of turbulence modeling for engineering prediction of swirling vortices in the near burner zone, International Journal of Heat and Fluid Flow 11 (3) (1990) 225 – 235, ISSN 0142-727X, doi:http://dx.doi.org/10.1016/0142-727X(90)90041-9.

[19] A. E. German, T. Mahmud, Modelling of non-premixed swirl burner flows using a Reynolds-stress turbulence closure, Fuel 84 (5) (2005) 583 – 594, ISSN 0016-2361, doi:http://dx.doi.org/10.1016/j.fuel.2004.10.015.

[20] H. Pitsch, H. Steiner, Large-eddy simulation of a turbulent piloted methane/air diffusion flame (Sandia flame D), Physics of Fluids (1994-present) 12 (10) (2000) 2541–2554, doi:http://dx.doi.org/10.1063/1.1288493.

[21] R. Kurose, H. Makino, Large eddy simulation of a solid-fuel jet flame, Combustion and Flame 135 (1Ũ2) (2003) 1 – 16, ISSN 0010-2180, doi: http://dx.doi.org/10.1016/S0010-2180(03)00141-X.

[22] A. Kempf, R. P. Lindstedt, J. Janicka, Large-eddy simulation of a bluff-body stabilized nonpremixed flame, Combustion and Flame 144 (1Ũ2) (2006) 170 – 189, ISSN 0010-2180, doi: http://dx.doi.org/10.1016/j.combustflame.2005.07.006.

[23] S. B. Pope, Turbulent flows, Cambridge University Press, 2000.

[24] H. Wengle, H. Werner, Large Eddy Simulation of Turbulent Flow over and around a Cube in a Plate Channel, in: Eight Symposium on Turbulent Shear Flows, Technical University of Munich, 1991.

[25] M. F. Modest, Radiative heat transfer, Academic Press, Burlington, 2 edn., 2003.

[26] T. F. Smith, Z. F. Shen, J. N. Friedman, Evaluation of coefficients for the weighted sum of gray gases model, Journal of Heat Transfer 104 (4) (1982) 602–608.

[27] M. F. Modest, H. Zhang, The Full-Spectrum Correlated-k Distribution for Thermal Radiation From Molecular Gas-Particulate Mixtures, Journal of Heat Transfer 124 (1) (2002) 30–38, doi:10.1115/1.1418697.

[28] J. Cai, M. F. Modest, Improved full-spectrum k-distribution implementation for inhomogeneous media using a narrow-band database, Journal of Quantitative Spectroscopy and Radiative Transfer 141 (2014) 65 – 72, ISSN 0022-4073, doi:http://dx.doi.org/10.1016/j.jqsrt.2014.02.028.

[29] M. F. Modest, R. J. Riazzi, Assembly of full-spectrum k-distributions from a narrow-band database; effects of mixing gases, gases and nongray absorbing particles, and mixtures with nongray scatterers in nongray enclosures, Journal of Quantitative Spectroscopy and Radiative Transfer 90 (2) (2005) 169 – 189, ISSN 0022-4073, doi:10.1016/j.jqsrt.2004.03.007.

[30] D. Poitou, J. Amaya, M. E. Hafi, B. Cuénot, Analysis of the interaction between turbulent combustion and thermal radiation using unsteady coupled LES/DOM simulations, Combustion and Flame 159 (4) (2012) 1605 – 1618, ISSN 0010-2180, doi: http://dx.doi.org/10.1016/j.combustflame.2011.12.016.

[31] M. Roger, P. J. Coelho, C. B. da Silva, Relevance of the subgrid-scales for large eddy simulations of turbulence-radiation interactions in

a turbulent plane jet, Journal of Quantitative Spectroscopy and Radiative Transfer 112 (7) (2011) 1250 – 1256, ISSN 0022-4073, doi: http://dx.doi.org/10.1016/j.jqsrt.2010.08.026.

[32] A. Gupta, D. Haworth, M. Modest, Turbulence-radiation interactions in large-eddy simulations of luminous and nonluminous nonpremixed flames, Proceedings of the Combustion Institute 34 (1) (2013) 1281 – 1288, ISSN 1540-7489, doi:10.1016/j.proci.2012.05.052.

[33] S. M. Godoy, F. C. Lockwood, Development of a two-colour infrared pyrometer for coal particle temperature measurements during devolatilisation, Fuel 77 (9-10) (1998) 995 – 999, ISSN 0016-2361, doi:10.1016/S0016-2361(97)00292-5.

[34] T. F. Wall, A. Lowe, L. J. Wibberley, T. Mai-Viet, R. P. Gupta, Fly Ash Characteristics and Radiative Heat Transfer in Pulverized-Coal-Fired Furnaces, Combustion Science and Technology 26 (3-4) (1981) 107–121, doi:10.1080/00102208108946951.

[35] A. L. Brown, T. H. Fletcher, Modeling Soot Derived from Pulverized Coal, Energy & Fuels 12 (4) (1998) 745–757, doi:10.1021/ef9702207.

[36] H. Chang, T. T. Charalampopoulos, Determination of the Wavelength Dependence of Refractive Indices of Flame Soot, Proceedings of the Royal Society of London. Series A: Mathematical and Physical Sciences 430 (1880) (1990) 577–591, doi:10.1098/rspa.1990.0107.

[37] O. Senneca, L. Cortese, Kinetics of coal oxy-combustion by means of different experimental techniques, Fuel 102 (2012) 751 – 759, ISSN 0016-2361, doi:http://dx.doi.org/10.1016/j.fuel.2012.05.033.

[38] I. W. Smith, The combustion rates of coal chars: A review, Symposium (International) on Combustion 19 (1) (1982) 1045 – 1065, ISSN 0082-0784, doi:http://dx.doi.org/10.1016/S0082-0784(82)80281-6.

[39] A. Pranzitelli, A. G. Clements, R. Porter, L. Ma, M. Pourkashanian, A. Duncan, Development and Application of a Novel Radiation Property Model for Oxy-Coal Combustion, in: Oxyfuel Combustion Conference 3, 2013.

[40] B. F. Magnussen, B. H. Hjertager, On mathematical modeling of turbulent combustion with special emphasis on soot formation and combustion, Symposium (International) on Combustion 16 (1) (1977) 719 – 729, ISSN 0082-0784, doi:http://dx.doi.org/10.1016/S0082-0784(77)80366-4.

[41] B. M. Visser, J. P. Smart, W. L. van de Kamp, R. Weber, Measurements and predictions of quarl zone properties of swirling pulverised coal flames, Symposium (International) on Combustion 23 (1) (1991) 949 – 955, ISSN 0082-0784, doi:http://dx.doi.org/10.1016/S0082-0784(06)80350-4.

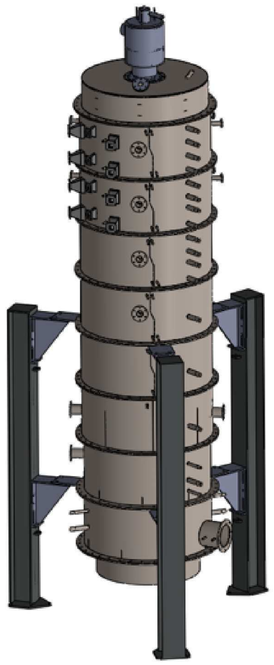

Figure 1: CAD image of the combustion test facility.

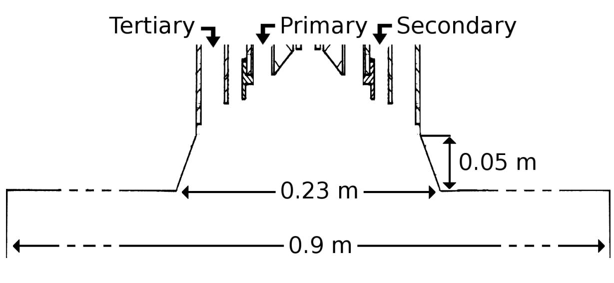

Figure 2: Sketch of the near burner region of the combustion rig.

El-Cerrejon coal properties	
Calorific values (MJ/kg)	
GCV	30.79
NCV	29.57
Proximate analysis (AR, wt. %)	
Fixed carbon	54.92
Volatiles	37.84
Ash	1.43
Moisture	5.81
Ultimate analysis (DAF, wt. %)	
C	79.31
H	5.43
N	2.67
S	0.40
O (by diff.)	12.19

Table 1: Details of the El-Cerrejon coal that was fired during the experimental measurements. The proximate analysis is reported 'as received' (AR), and the ultimate analysis is reported on a dry ash-free (DAF) basis. Oxygen content is calculated by difference.

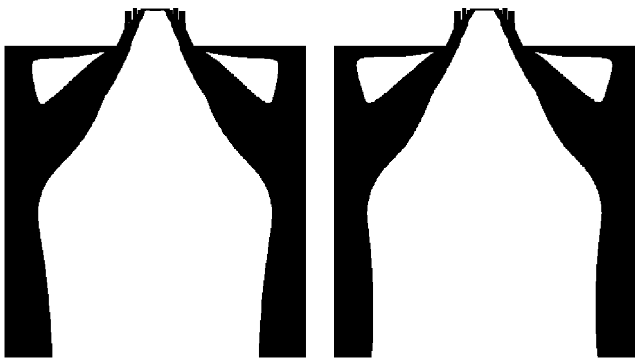

(a) Air (b) Oxyfuel

Figure 3: Grid resolution criteria for the two cases in the near-burner region. Shaded areas indicate regions in which the cell size is too coarse to resolve 80% of the turbulent scales, as predicted by the RANS solutions.

	Air	Oxy-27
Mass flow rate (kg/hr)		
Fuel	24.4	24.4
Primary	55.7	59.8
Secondary	95.9	102.4
Tertiary	129.2	129.2
Inlet gas temperature (K)		
Primary	293	294
Secondary	524	517
Tertiary	524	517
Oxygen concentration (vol. %)		
Primary	20.95	17.95
Secondary	20.95	29.24
Tertiary	20.95	29.24
Approximate furnace pressure (Pa)		
	-100	-130

Table 2: Inlet flow rates and gas compositions that were used for the CFD calculations. The balance of the gas compositions in the oxyfuel case was made up of CO_2. The furnace pressure is relative to ambient pressure.

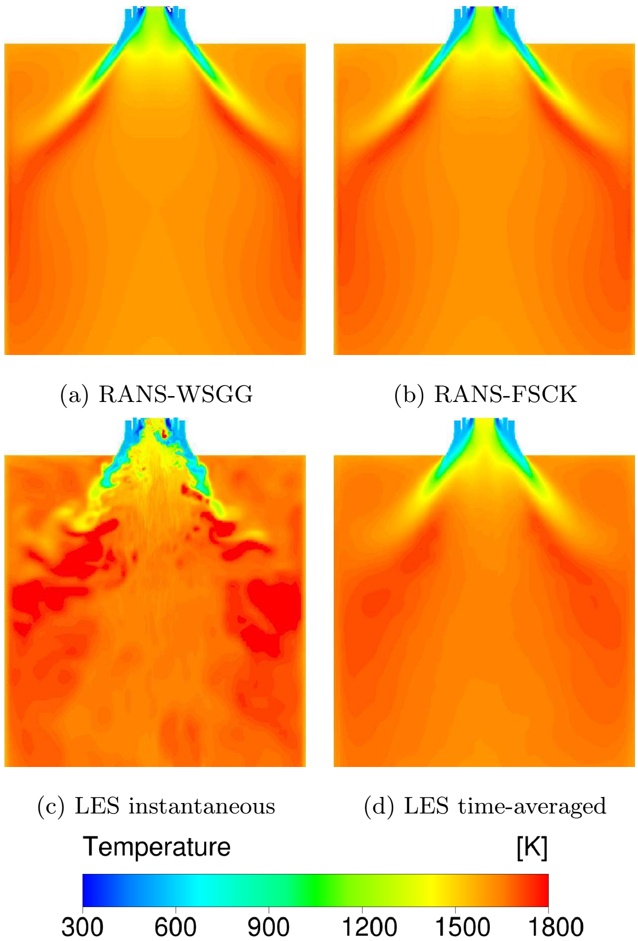

(a) RANS-WSGG

(b) RANS-FSCK

(c) LES instantaneous

(d) LES time-averaged

Figure 4: Temperature distributions for the air-fired case.

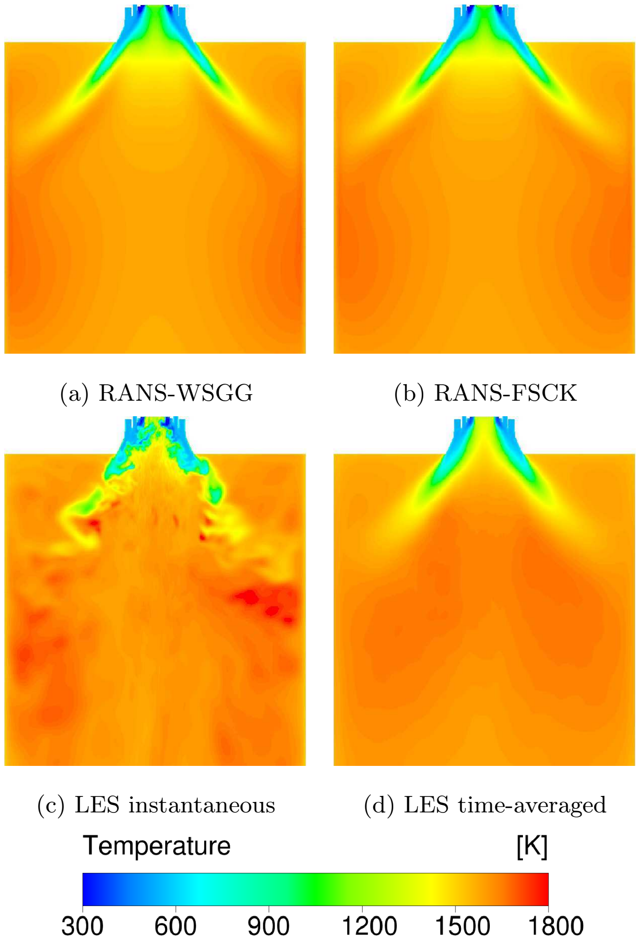

Figure 5: Temperature distributions for the oxyfuel case.

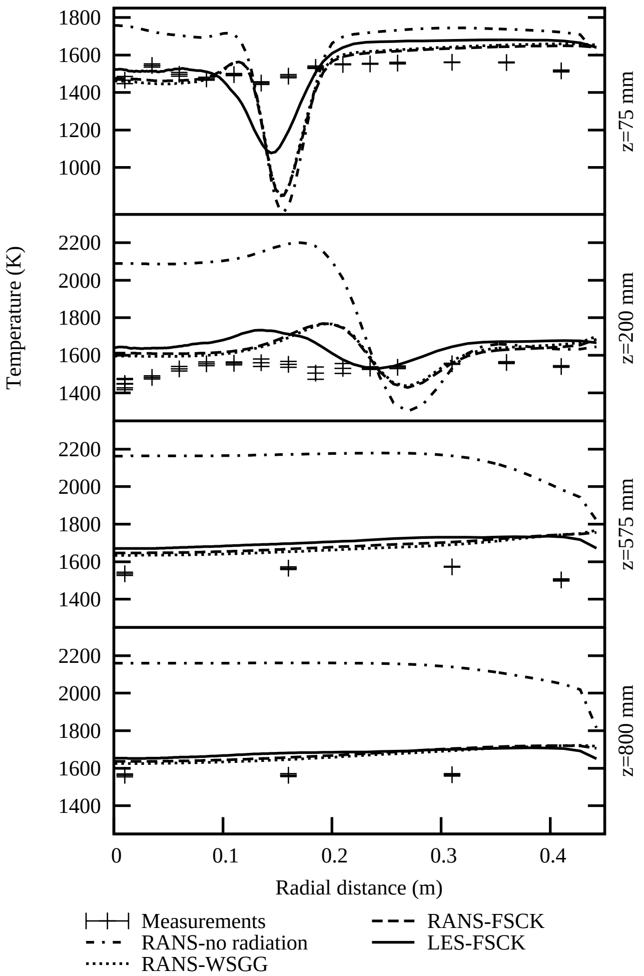

Figure 6: Radial temperature plots for the air-fired CFD cases alongside suction pyrometry measurements. In the figure, z represents the distance from the quarl exit.

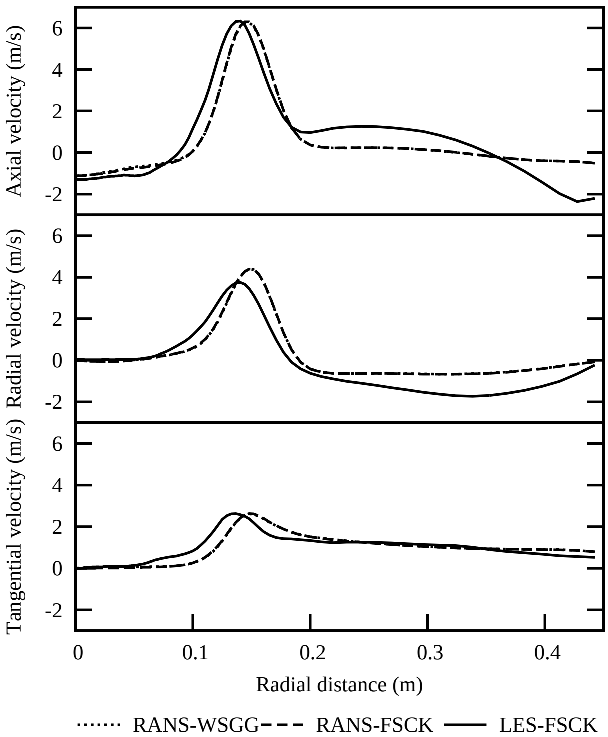

Figure 7: Plots of the time-averaged axial, radial and tangential velocities in the near burner region for the air-fired case (z=75 mm).

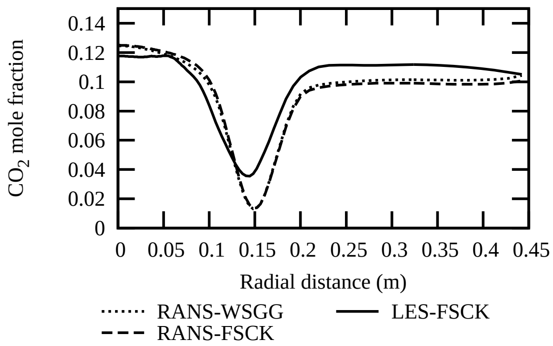

(a) CO_2 mole fraction

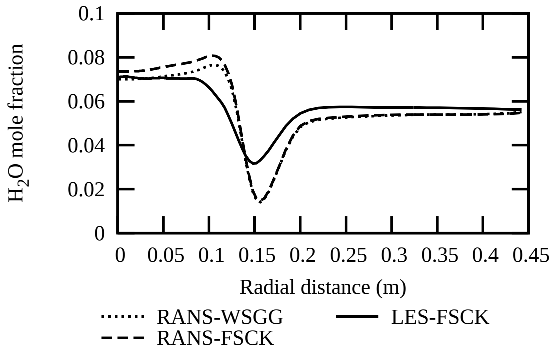

(b) H_2O mole fraction

Figure 8: Distribution of the participating species close to the burner (z=75 mm) for the air-fired case.

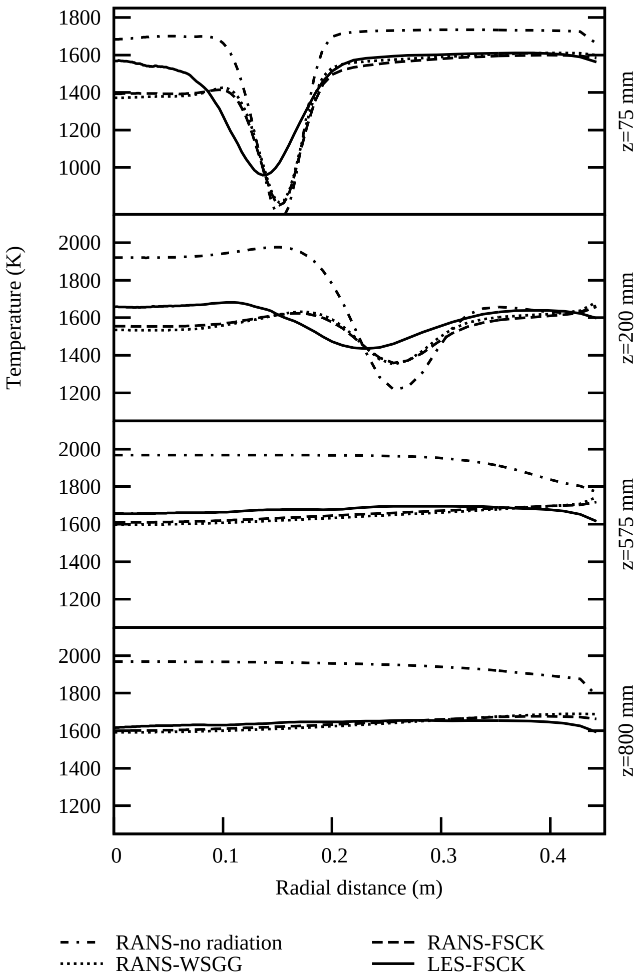

Figure 9: Radial temperature plots for the oxy-27 CFD cases. In the figure, z represents the distance from the quarl exit.

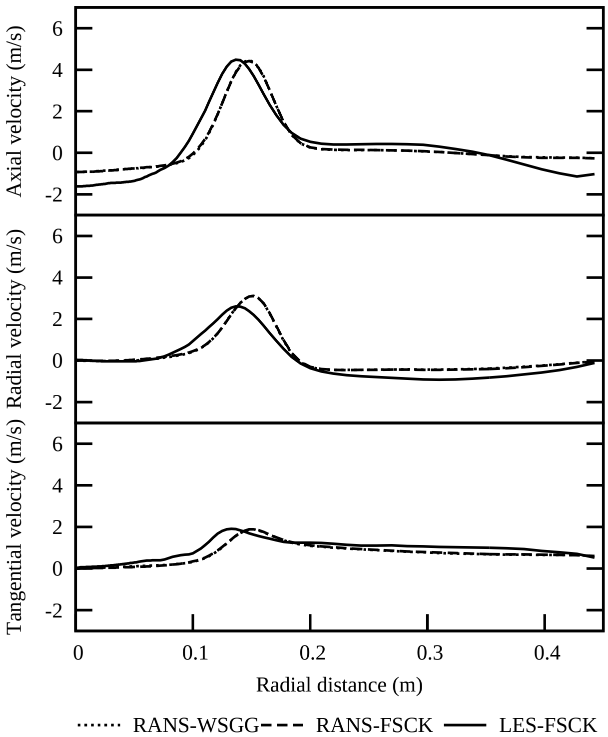

Figure 10: Plots of the time-averaged axial, radial and tangential velocities in the near burner region for the oxyfuel case (z=75 mm).

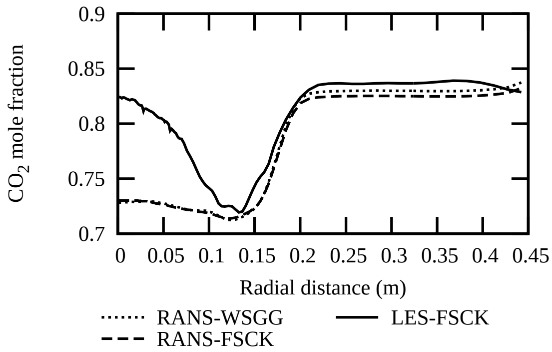

(a) CO_2 mole fraction

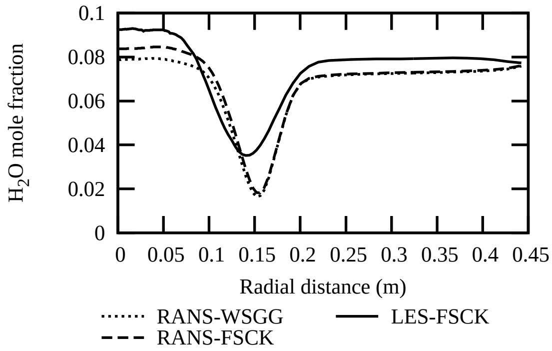

(b) H_2O mole fraction

Figure 11: Distribution of the participating species close to the burner (z=75 mm) for the oxyfuel case.

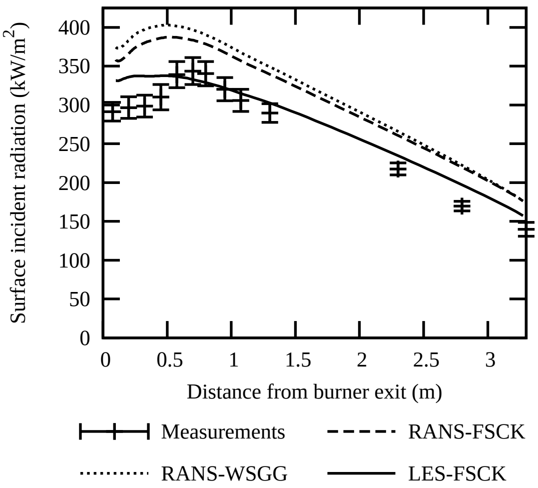

Figure 12: Surface incident radiation for the air-fired CFD cases alongside experimental measurements. Measurements were taken down the height of the furnace. Points represent the time-averaged mean measurement value, with error-bars representing one standard deviation of the values and a 3% error margin quoted from the probe manufacturer.

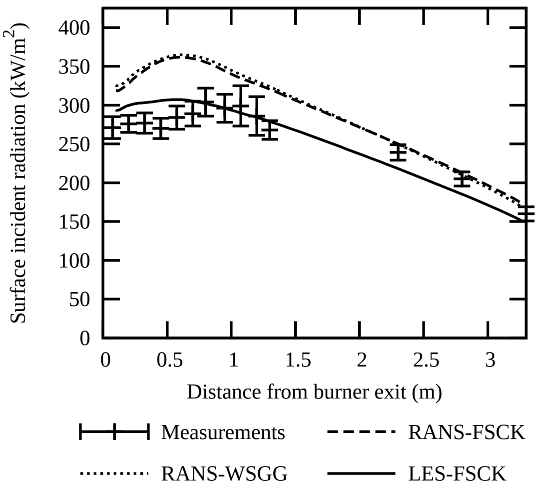

Figure 13: Surface incident radiation for the oxy-27 CFD cases alongside experimental measurements. Measurements were taken down the height of the furnace. Points represent the time-averaged mean measurement value, with error-bars representing one standard deviation of the values and a 3% error margin quoted from the probe manufacturer.